SURFACE MICROMACHINED BRIDGE CONFIGURATIONS FOR ACCURATE ANGLE MEASUREMENTS

Jörg R. Kaienburg, Michael Huonker, and Ralf Schellin
Automotive Equip. Div. 8, Dept. K8/SPP, Robert Bosch GmbH
P.O.B. 13 42, D-72703 Reutlingen, Germany
email: joerg.kaienburg@bosch.com

ABSTRACT

This paper reports on new sensing elements and the corresponding read-out circuit of a novel silicon surface micromachined angle sensor. Different bridge configurations – half and full bridges – comprising up to four variable capacitors were designed and characterized. The combination of such array-like arrangements and further improved sensing elements lead to a significant increase of performance. In this paper modeling, the evaluation circuit, and experimental results of different bridge configurations are presented.

INTRODUCION

Accurate angle measurements are very important for many and totally different applications, e. g. automotive security or operational monitoring systems. Severe working conditions and demands for long-lasting and wear-free functionality give reason for contactless detection methods. Low cost is a further essential goal which can be reached by using standard and batch processes. Hence, this angle sensor was designed to interact via Lorentz force with a given magnetic field and was fabricated using Bosch's standard silicon surface micromachining process.

Other solutions fulfilling the requirements above are well known, for instance sensors using optical [1], capacitive [2], or inductive pick-up methods. But the most related sensors are those, which are based upon the hall [3, 4], anisotropic magneto-resistance [5, 6], or the giant magneto-resistance effect [7]. No matter what kind, all sensors measure the same quantity: the angle α enclosed by a predominant direction, e. g. the easy axis in AMR-devices, and the direction of the external magnetic field. But these sensors have still some drawbacks implying individual trade-offs. For instance, temperature affects the output signal, the offset, and, hence, the performance of the whole system of such sensors.

PRINCIPLE OF OPERATION

Basically, one sensing element consists of a movable polysilicon structure which is suspended by torsional bars forming a micromechanical pendulum (Fig. 1). The main parts of such a sensing element are a conducting frame defining the path of the fed current and being used as excitation coil, a paddle structure serving as the middle electrode of a differential capacitor, two lower electrodes fixed to the substrate, and torsion bars suspending the whole sensing element and defining the torsion axis A. Paddle structure and fixed electrodes are building a rotatory differential capacitor, C_1 and C_2, enabling a signal transformation via amplitude modulation of fed carrier voltages (Fig. 2). Each sensing element is fed by a current $\vec{I}_{se}$ of typically 1 mA that interacts with an external magnetic field $\vec{B}$ of roughly 100 mT. Helmholtz coils or permanent magnets are used to generate this magnetic field.

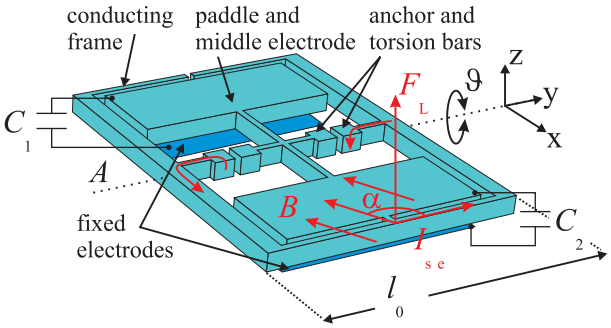

Figure 1: Schematic view of a sensing element (B1-type). A current I_{se} is fed using the suspending torsion bars as conductors and interacts with a given magnetic field B.

The resultant Lorentz force

$$\vec{F}_L = l_0 \cdot \vec{I}_{se} \times \vec{B} \quad (1)$$

$$= l_0 I_{se} B \sin(\alpha) \cdot \vec{e}_z \quad (2)$$

yields a torque

$$\vec{M}_L = \vec{r}_L \times \vec{F}_L \quad (3)$$

$$= r_L l_0 I_{se} B \sin(\alpha) \underbrace{\sin(\pi/2 - \vartheta)}_{\approx 1} \cdot \vec{e}_y \quad (4)$$

that deflects the sensing element. This deflection is a tilting motion around the torsion axis A described by the torsion angle ϑ with respect to the substrate plane. A further deflecting torque on the basis of at-

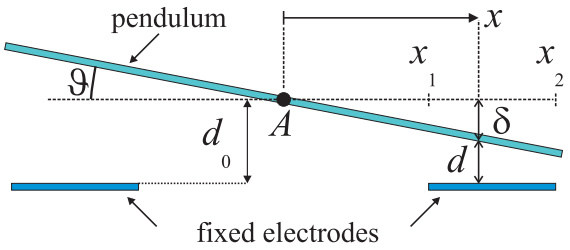

Figure 2: Side face sketch of the tilting motion ϑ and its influence upon the deflection $\delta(x,\vartheta) = x\tan(\vartheta)$ at the distance x from the torsion axis.

tractive Coulomb forces results if potential drops U between middle and fixed electrodes occur. Considering the interrelationship between distance x from the torsion axis and deflection $\delta(x)$ as depicted in Fig. 2, this turning moment can be constituted as

$$M_{\mathrm{el}} = 2\,\varepsilon_0\,y_{\mathrm{c}}\,U^2 d_0\tan(\vartheta) \cdot \int_{x_1}^{x_2} \frac{x^2\left[3\,d_0^2 + x^2\,\tan^2(\vartheta)\right]}{\left[d_0 - x\tan(\vartheta)\right]^3\left[d_0 + x\tan(\vartheta)\right]^3}\,dx \tag{5}$$

where ε_0 is the permittivity of free space and y_{c} the dimension of the electrodes in y-direction.

The only repulsive torque is generated by the torsional motion of the torsion bars in cases of deflection

$$\vec{M}_\vartheta = \kappa_{\mathrm{res}}\,\vartheta\cdot(-\vec{e}_{\mathrm{y}}) \tag{6}$$

where κ_{res} is the resulting stiffness of torsion of all suspending torsion bars. For a single bar its stiffness of torsion is defined as

$$\kappa = \frac{1}{3}\,\beta\,G\,\frac{w^3 h}{l} \tag{7}$$

where w is the bar's width, h its height, l its length, G the shear modulus, and

$$\beta = 1 - \frac{192\,w}{\pi^5\,h}\sum_{n=1}^{\infty}\frac{1}{2\,n-1}\,\tanh\left[\frac{(2\,n-1)h\,\pi}{2\,w}\right] \tag{8}$$

a scalar valid for rectangular cross sections and depending on the ration $h : w$. The equilibrium state is defined by the following equation

$$M_\vartheta = M_{\mathrm{L}} + M_{\mathrm{el}} \approx M_{\mathrm{L}} \tag{9}$$

Minimizing the potential drop U between the electrodes allows to neglect the electrostatic torque. A

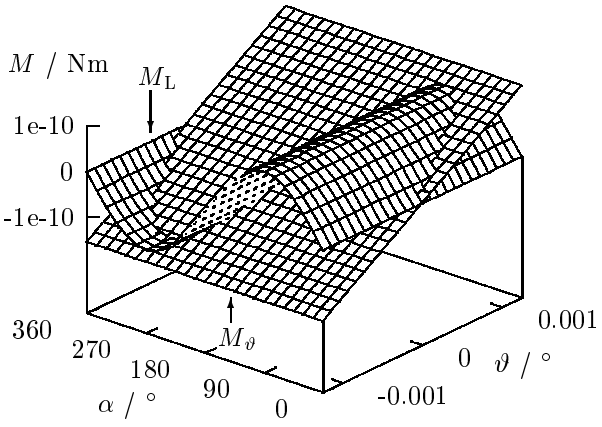

Figure 3: Visualization of Eq. 9 for a B2-type angle sensor (Tab. 1). The sinusoidal surface describes the deflecting Lorentz torque, and the repulsive torque is displayed as a tilted plane, where its slope is the stiffness of torsion. By this, the intersection represents the resultant torsion angle $\vartheta(\alpha)$ (Eq. 10).

solution of Eq. 9 for the resultant torsion angle $\vartheta(\alpha)$ can be found easily

$$\vartheta(\alpha) = \frac{3\,r_{\mathrm{L}}\,l_0\,I_{\mathrm{se}}\,B}{\beta\,G}\,\frac{l}{w^3 h}\,\sin(\alpha) \tag{10}$$

where α is the angle enclosed by $\vec{I}$ and $\vec{B}$ and, of course, the quantity to be measured. Both detection capacitors $C_1(\alpha)$ and $C_2(\alpha)$ vary in a counterphase manner. The values of both sense capacities can be calculated via

$$C_{1,2}(\alpha) = \varepsilon_0\,y_{\mathrm{c}}\int_{x_1}^{x_2}\frac{1}{d_0 \pm x\,\tan\left(\vartheta(\alpha)\right)} \mp \frac{x\,\tan\left(\vartheta(\alpha)\right)}{\left[d_0 \pm x\,\tan\left(\vartheta(\alpha)\right)\right]^2}\,dx \tag{11}$$

The sensing elements were designed to obtain a $\triangle C/C$ of roughly ± 11 % in the cases of approximating and spreading electrodes.

Although $C_1(\alpha)$ and $C_2(\alpha)$ show no sinusoidal dependence on α, their difference $C_1(\alpha) - C_2(\alpha)$ does (Fig. 4). A sinusoidal shape of the finally resulting output voltage can be predicted. Moreover, the essential proportionality valid for $C_1(\alpha) - C_2(\alpha)$ is

$$C_1(\alpha) - C_2(\alpha) \propto I_{\mathrm{se}}\,B\,\sin(\alpha) \tag{12}$$

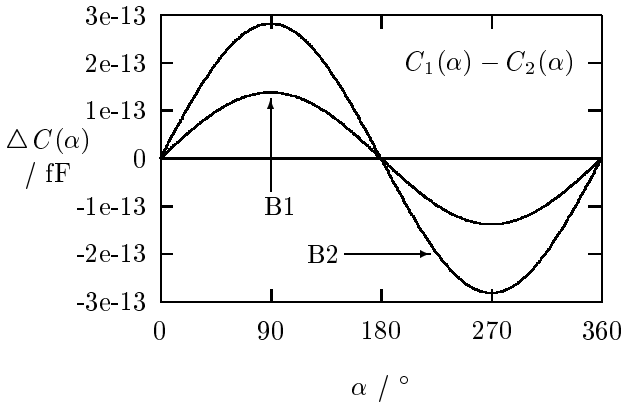

Figure 4: Calculated difference $C_1(\alpha) - C_2(\alpha)$ of a half bridge's sense capacitors $C_1(\alpha)$ and $C_2(\alpha)$ (I_{se} = 1 mA, B = 100 mT).

BRIDGE CONFIGURATIONS

All sensor chips were fabricated using the silicon surface micromachining process of Robert Bosch GmbH, Germany [9, 10]. The core idea of a bridge configu-

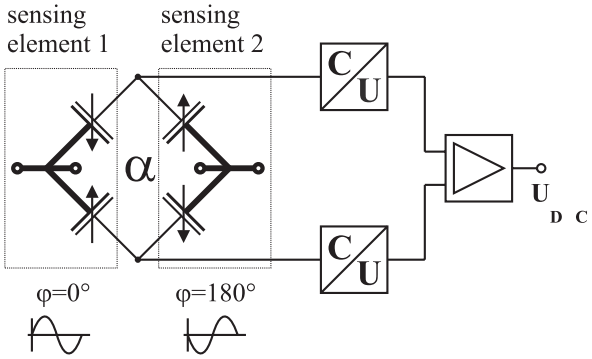

Figure 5: Schematic view of the core idea. A half bridge is built out of two sensing elements (boldfaced printed) and one fixed counter-electrode per element. Both half bridges combined as depicted yield a full bridge. The supplies of the sensing elements are indicated by terminals.

ration in surface micromachining is choosing sensing elements as movable middle electrodes of differential capacitors in combination with pairs of fixed electrodes, where one electrode belongs to one sensing element and the other to another sensing element (Fig. 5). At their contact an addition of any signal is forced. Each bridge (Tab. 1) uses this to sum carrier voltages which were fed into the movable sensing elements and cross-talked to the fixed electrodes. As indicated in Fig. 5, carrier voltages of the same amplitude (300 mV) and frequency (60 kHz) but a phase shift of 180° were utilized. Hence, in the home

sensor type (kind of bridge configuration)	measuring range
B1 (2 half bridges)	-90° to +90°
B2 (1 full bridge)	-90° to +90°

Table 1: Survey of realized bridge configurations.

position of the pendulums both signals are added to zero. The sensing elements of every bridge configuration fulfill the condition of an antiphase deflection in comparison to its adjacent sensing elements. This results in an antiphase amplitude modulation of the fed carrier voltages, especially at the summation points. These summation points are contacted with the first stage of the read-out electronics performing C/U-converters.

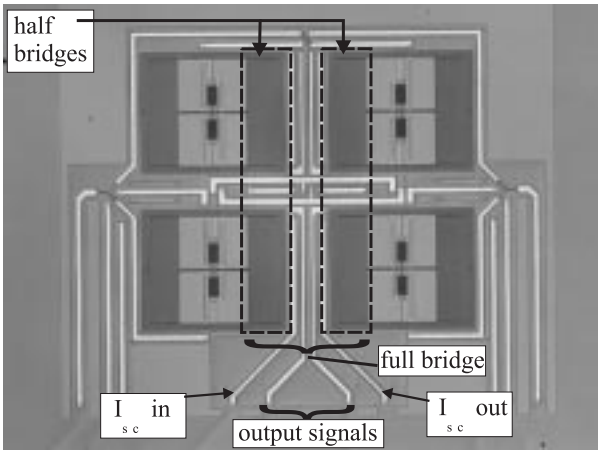

Figure 6: Complete sight of a B1-type angle sensor chip. Four sensing elements are arranged in pairs of half bridges. Carrier voltages were fed using the outer tracks.

As can be distinguished clearly in Fig. 6 and Fig. 7, B1 differs significantly from B2. In a B1-type sensor chip four sensing elements are arranged in pairs of half bridges, where only the inner capacitor of each serves as a capacitor in the resultant bridges. The other capacitors could be used for a redundant angle detection or for testing.

Two pendulums are placed building a full bridge in B2-type chips (Fig. 7). This enables a space-saving mounting of another full bridge mutually perpendicular in plane for a 360°-detection of the given angle α (so-called B3-type, still under investigation). Despite this and the extended interconnection inside the sensor chip, B2- and B3-types are identical.

The main difference between B1- and B2-type sensing elements can be found in the suspension. This correlates to a design modification of the frame and

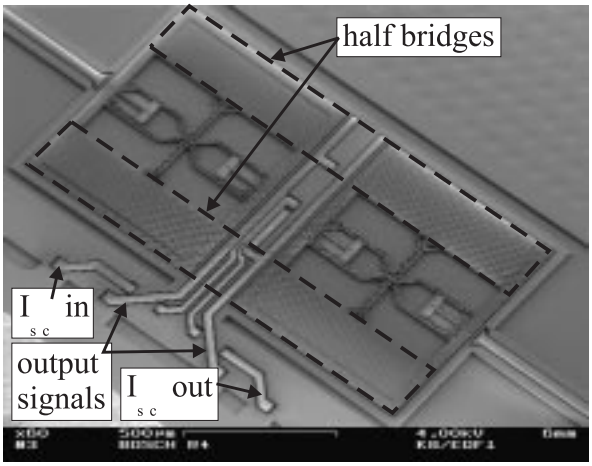

Figure 7: Complete view of a B2-type full bridge configuration inside the sensor chip. Two discrete tracks – upper left and lower right corner – are used for feeding the carrier voltages.

the paddle. The sensing elements of a B1-type sensor are constructed as depicted in Fig. 1. The current I_{se} flows through only one half of the sensor, so a Lorentz force is generated on only one side of the torsion axis A (here: frame = excitation coil with 1/2 winding). A duplication of the deflecting Lorentz torque was realized by a twin bar suspension of B2-type pendulums (here: frame = excitation coil with 1 winding).

Both sensor types were fed with a current I_{sc} by supplying a voltage at the input terminals (via bondpads wire-bonded to the current control loop). Due to the arrangement of n sensing elements ($n \in \{2, 4\}$), the n-th part I_{se} of the fed current I_{sc} flows through every single sensing element ($I_{\mathrm{se}} = 1/n \cdot I_{\mathrm{sc}}$). Therefore precise designs were necessary to attain the same resistance for each sensing element.

B1 and B2 have in common that their paddles are contacted to the frame where the potential drop along the frame reaches roughly 0 V. Small deviations are leveled out by the evaluation circuit. Hence, potential drops from the middle electrode to both fixed electrodes underneath are minimized or even eliminated. The carrier voltages were fed using the outer tracks to suppress cross-coupling as far as possible (Fig. 6 and 7).

EVALUATION CIRCUIT

In Fig. 8 the block diagram of a complete sensor is shown. It is designed in modular system. The main signal path consists of a signal source (indicated as f_c), the sensor chip, and the read-out circuit comprising an amplification followed by a synchronous demodulation and a low pass filter. C/U-converters and a succeeding differential amplification build the amplification stage (Fig. 5). The output voltage U_{out} is a d.c. voltage only varying sinusoidally with the given angle α

$$U_{\mathrm{out}} \propto \sin(\alpha) \tag{13}$$

The amplitude of this output signal depends on the design of the sensing elements, the used current I_{se} and magnetic field B, and on the analogous read-out circuit. Additionally, an optional offset trimming of U_{out} is provided with the low-pass filter.

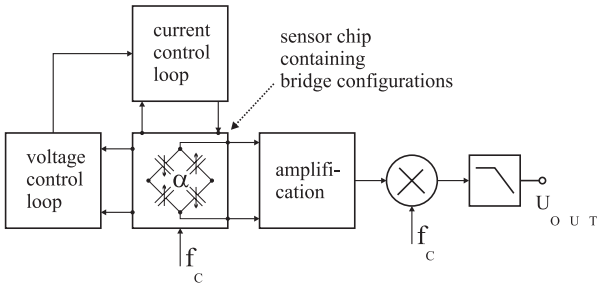

Figure 8: Block diagram of the evaluation circuit appropriate for B1- and B2-types.

Special control loops were implemented to guarantee constant currents and negligible electrostatic coupling effects. The current I_{se} which is necessary to

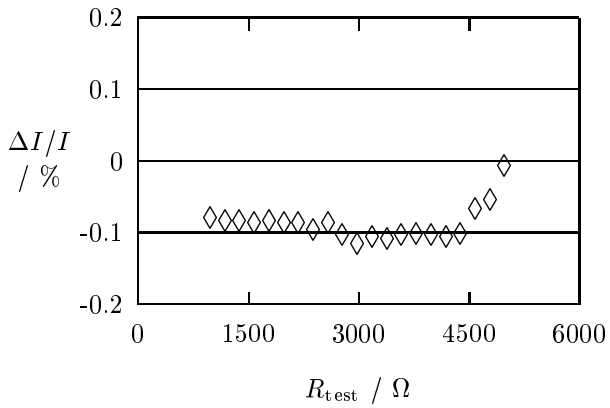

Figure 9: Very small relative deviation of the sensor chip's bias current I_{sc} with respect to a large variation of a test resistance R_{test} substituting the sensor chip resistance R_{sc}.

generate the Lorentz force is created by applying a voltage U_{ccl} to the sensor chip. Depending on the used sensor chip, slight variations of the resultant chips' resistances occur. These variations are leveled out by the current control loop with current deviations of below 0.11 % by adapting U_{ccl} automatically (Fig. 9). Depending on the specific resistance of each sensor chip, different voltages must be supplied to

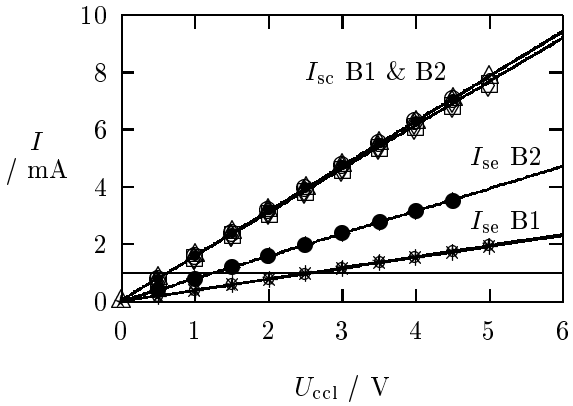

Figure 10: Characteristic lines of the sensor chip and sensing element currents I_{sc} and I_{se} dependent on the voltage U_{ccl} of the current control loop.

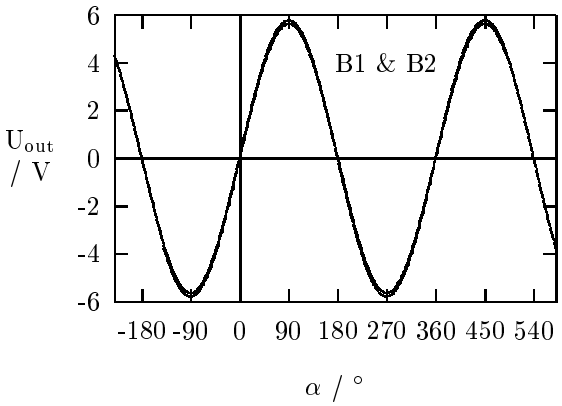

Figure 11: Comparison of B1- and B2-type sensors' output signals. Slight differences in the circuits amplifications are responsible for the small mismatch of the output curves. By design, the predominant direction of B2-type sensor is orthogonal oriented compared to B1-type sensors.

gain the needed currents through the sensor chips. It is obvious, that due to the difference in resistance of B1- and B2-type sensor chips different sensing element currents I_{se} result although roughly the same sensor chip currents I_{sc} are fed (Fig. 10). Therefore, higher possible currents I_{se} through B2-types lead to higher sensitivities and resolutions.

The voltage control loop measures the voltage drop U between paddle and lower electrodes. To avoid significant electrostatic coupling effects, this control loop was designed to shift the voltage U_{sc} applied to the sensor chip parallel at its both current input terminals until the measured voltage drop is leveled to zero. Hence, the applied voltage can be written as a superposition of U_{ccl} and U_{vcl}

$$U_{sc} = U_{ccl} + U_{vcl} \tag{14}$$

where U_{vcl} is the voltage of the voltage control loop.

EXPERIMENTAL RESULTS

Typical output signals of B1- and B2-types are shown in Fig. 11. For clearity, only measured signals (1°-steps) are shown in this plot, because a theoretical or fitted curve couldn't be distinguished. Their maximum deviation from a strongly sinusoidal fit-function (method based upon the Levenberg-Marquardt algorithm)

$$f(x) = A \sin\left((\alpha - \alpha_c)\,\frac{\pi}{\Phi}\right) \tag{15}$$

is understood as the accuracy (in degrees). Here A, α_c, and Φ are fit parameters representing amplitude, phase shift, and period in degrees, respectively. The amplitude is affected by the bias current I_{sc}, the magnetic field B, and the circuit's alignment. The experimental setup is responsible for the angle offset α_c. The obtained periods Φ are $179.8 \pm 0.4°$, so a good agreement with the theory could be deduced. Beside the accuracy, sensitivity, signal to noise ratio, and resolution are further interesting quantities, especially in the small angle range $\alpha \in [-10°; 10°]$ where linear behaviour of the output voltage could be observed. Sensitivity is defined as

accuracy	observed	expected
B1-type	0.55	< 0.1
B2-type	0.41	< 0.1

Table 2: Measured and expected accuracies of both sensor types.

$$S_\alpha = \frac{\triangle U_{out}}{\triangle \alpha} \tag{16}$$

$$S_{\alpha,max} = S_\alpha|_{\alpha=0°} \tag{17}$$

Due to the sinusoidal shape of U_{out} the resultant sensitivity depends on the angle α until it vanishes at $\alpha = 0° + n \cdot 180°$ ($n \in \{\ldots, -2, -1, 0, 1, 2, \ldots\}$).

If U_n is the noise voltage of the complete sensor, a signal to noise ration (SNR) – depending on α too – could be written as

$$SNR|_{\triangle\alpha} = 20 \log\left(\frac{S_\alpha}{U_n} \cdot \triangle\alpha\right) \tag{18}$$

$$SNR_{max} = SNR|_{\alpha=0°} \tag{19}$$

Its reciprocal

$$R_{\triangle\alpha} = \frac{1}{SNR|_{\triangle\alpha}} \cdot 1° \tag{20}$$

$$R_{\alpha,max} = R_\alpha|_{\alpha=0°} \tag{21}$$

is understood as the resolution of the sensor. In Tab. 3 observed sensitivities, signal to noise ratios, and resolutions are summarized.

	S_α / mV/°	SNR / dB	R_α / °
B1-type	50	40	0.01
B2-type	90	45	0.006

Table 3: Measured sensitivity, signal to noise ratio, and resolution of each sensor type (operational point: $\alpha = 0°$, $I_{se} = 1$ mA, $B = 100$ mT, bandwidth $f_g = 50$ Hz).

CONCLUSION

A new set of sensing elements of a novel angle sensor has been developed. In combination with a special evaluation circuit the sensor performance has been improved significantly in comparison to the first generation [8]. Output signals of the C/U-converters have been increased by nearly two orders of magnitude. The sensors signal to noise ratio has been optimized to 45 dB enabling a maximum resolution of 0.006 ° (operating point: $\alpha = 0°$, $\triangle\alpha = 1°$, $I_{se} = 1$ mA, $B = 100$ mT, $f_g = 50$ Hz). Accuracies of 0.41° and 0.55° were reached for both sensor designs.

Future work is aiming for a more detailed model taking into account process variations and electrostatic coupling effects. Improving the accuracy by at least one order of magnitude is another important goal of further investigations.

ACKNOWLEGDEMENTS

The authors would like to thank the foundry- and FAB-teams for organizing and processing the wafers and S. Fleiner, M. Weimar, and R. Benz for a sophisticated preparation of all devices. H. Kittel, D. Heisenberg, and R. Galster are acknowledged gratefully for putting their measuring desk at our disposal. Finally, we want to express our thank to Prof. H. Sandmaier, J. Marek, and G. Bischopink for their support.

References

[1] T. A. Kwa and R. F. Wolffenbuttel, *Optical angular displacement sensor with high resolution integrated in silicon*, Sensors and Actuators A 32, 1992, pp. 591–597.

[2] R. F. Wolffenbuttel and R. P. van Kampen, *An integrable capacitive angular displacement sensor with improved linearity*, Sensors and Actuators A 25-27, 1991, pp. 835–843.

[3] R. S. Popovic, *Hall devices for magnetic sensor microsystems*, Proc. Transducers '97, Chicago, 1997, pp. 377–380.

[4] F. Burger, P.-A. Besse, R. S. Popovic, *New fully integrated 3-D silicon Hall sensor for precise angular-position measurements*, Sensors and Actuators A 67, 1998, pp. 72–76.

[5] C. J. M. Eijkel, J. H. J. Fluitman, H. Leeuwis, and D. J. M. van Mierlo, *Contactless angle detector for control applications*, 3T Twente Technology Transfer BV, Enschede, The Netherlands, 1997.

[6] S. Pusch, *Integrated angle sensor based on the magnetoresistive effect*, Philips Semiconductors - Systems Lab. Hamburg, Proc. SENSOR '97, Vol. 1, 1997, pp. 37–42.

[7] K.-M. H. Lenssen, D. J. Adelerhof, H. J. Gassen, A. E. T. Kuiper, G. H. J. Somers, and J. B. A. van Zon, *Robust giant magnetoresistance sensors*, Philips Res. Lab., Eindhoven, The Netherlands, Proc. Eurosensors XIII, 1999, pp. 589–596.

[8] J. Kaienburg, M. Lutz, B. Maihöfer, and R. Schellin, *A precise and contactless angle detection sensor using surface micromachining technology*, Proc. MEMS '98, 1998, pp. 367–371.

[9] M. Offenberg, H. Münzel, D. Schubert, O. Schatz, F. Lärmer, E. Müller, B. Maihöfer, and J. Marek, *Acceleration sensor in surface micromachining for airbag applications with high signal/noise ratio*, SAE 960758, 1996, pp. 35–41.

[10] M. Offenberg, *Industrial foundry for surface-micromachined sensors*, MST-News, Vol. 15, 1996, p. 4